Drying regimes in homogeneous porous media from macro- to nanoscale

J. Thiery,[1,2] S. Rodts,[2] D. A. Weitz,[1] and P. Coussot[2,*]

[1]*Experimental Soft Condensed Matter Group, School of Engineering and Applied Sciences, Harvard University, Cambridge, Massachusetts 02138, USA*

[2]*Université Paris-Est, Laboratoire Navier (ENPC-IFSTTAR-CNRS), Champs sur Marne 77420, France*

(Received 10 February 2017; published 25 July 2017)

Magnetic resonance imaging visualization down to nanometric liquid films in model porous media with pore sizes from micro- to nanometers enables one to fully characterize the physical mechanisms of drying. For pore size larger than a few tens of nanometers, we identify an initial constant drying rate period, probing homogeneous desaturation, followed by a falling drying rate period. This second period is associated with the development of a gradient in saturation underneath the sample free surface that initiates the inward recession of the contact line. During this latter stage, the drying rate varies in accordance with vapor diffusion through the dry porous region, possibly affected by the Knudsen effect for small pore size. However, we show that for sufficiently small pore size and/or saturation the drying rate is increasingly reduced by the Kelvin effect. Subsequently, we demonstrate that this effect governs the kinetics of evaporation in nanopores as a homogeneous desaturation occurs. Eventually, under our experimental conditions, we show that the saturation unceasingly decreases in a homogeneous manner throughout the wet regions of the medium regardless of pore size or drying regime considered. This finding suggests the existence of continuous liquid flow towards the interface of higher evaporation, down to very low saturation or very small pore size. Paradoxically, even if this net flow is unidirectional and capillary driven, it corresponds to a series of diffused local capillary equilibrations over the full height of the sample, which might explain that a simple Darcy's law model does not predict the effect of scaling of the net flow rate on the pore size observed in our tests.

DOI: 10.1103/PhysRevFluids.2.074201

I. INTRODUCTION

Drying of micro- and nanoporous media is essential to a plethora of industrial processes such as the synthesis of drugs and cosmetics in the pharmaceutical sector, the treatment of soils in agriculture and oil recovery, and the use of concrete, plasters, and paints in the building industry. Although the understanding of this process is critical for minimizing energy consumption and controlling the final material properties, its scientific description is challenging as it involves a transient, spatially heterogeneous phase transition.

The basic phenomenological mechanisms of drying in simple systems initially filled with pure liquid have been identified [1–7]. After a short induction period of variable duration, a constant drying rate period (CRP), associated with a homogeneous desaturation of the medium, usually occurs. In particular, in this regime capillary equilibration processes allow for water redistribution throughout the whole medium [1,8–11]; since the vapor density conditions are approximately conserved around the surface of evaporation of the sample the apparent constant drying rate is preserved. This regime is followed by a falling drying rate period (FRP) and more or less simultaneously the appearance of a heterogeneous saturation profile [1,8–11]. There is a critical interest in this transition in practice as it reveals tendencies to water retention and shows a possible dramatic decrease of the drying rate. The exact conditions for this FRP to start as well as the evolution of the liquid distribution within

*philippe.coussot@ifsttar.fr

the medium in this regime are not yet well determined and understood, except in the case of gravity dominated flow, with a focus on soils [12–16]. It is generally considered that the onset of this second regime results from a demand of liquid, through the imposed evaporation rate, larger than the liquid flux towards the free surface and resulting from capillary effects. Such a situation would lead the inward growth of a dry region from the sample free surface [1,4,7]. In detail, it was also suggested that two FRPs should be considered [4,17–19], associated with the continuous and the discontinuous states of the liquid network. The development of a receding dry front was observed and measured in a variety of cases, such as experiments with a nonwetting liquid [20], accumulation of ions [21] or particles [22,23] below the free surface, a packing filled with a paste [10], and a packing of large beads [23], and in all cases the drying rate in this second regime was probed to scale as the diffusion of vapor from the wet front to the free surface. However, due to the limited possibilities of internal observations, up to now we have ignored what determines this transition, what are the processes of liquid flow in that period, and what is the impact of the porous media characteristics (e.g., pore size) on these phenomena.

In this work, we use a magnetic resonance imaging (MRI) profiling technics to gain access to the liquid distribution in time within model porous media with pore size covering almost four decades down to the nanometer scale. This measurement enables one to characterize the physical processes governing drying in the FRP regime and in particular to investigate the dynamics of liquid and vapor transport in these model systems.

This paper is organized as follows. In Sec. II we describe the materials synthesized and the measurement tool used. Section III aims at presenting a discussion of our results and models; eventually, our conclusion is featured in Sec. IV.

II. MATERIALS AND METHODS

A. Materials

We focus on the simplest model porous media, i.e., bead packings, in the form of particulate gels with a solid volume fraction (i.e., $\phi_0 = 58 \pm 3\%$) approaching the maximum (disordered) value. These gels are made of amorphous aggregated and almost monodispersed silica particles of diameter $2R = 6$, 12, and 40 nm (Ludox SM-30, HS-40, and TM-40, respectively, provided by Sigma-Aldrich) or of diameter $2R = 80$, 300, 1000, and 1500 nm (provided by Fiber Optics Center), suspended in water. The deviation from nominal size was measured to 6% on average. Also, we manufactured a sample with $2R = 45$ μm glass beads by pressing and heat-sintering beads together. Note that silica and glass both have hygroscopic surfaces.

For bead diameters of 40 nm and smaller the samples are initially prepared as gels with a solid fraction of 20%. These gels are further dried on a nonadhering substrate, allowing them to shrink in a homogeneous manner under the action of capillary forces [24]. During shrinkage the gels remain saturated [24,25]; however, when shrinkage stops, the sample starts to desaturate—this regime constitutes the stage of interest within the present frame. Using MRI, we previously demonstrated our ability to distinguish between the saturated and nonsaturated regimes during this process [25]. Here we show only the saturation profiles starting from the last saturated profile recorded, i.e., just at the end of the homogeneous shrinkage. At that time, we observed that the sample concentration was around 58%.

Samples made with a bead diameter of 80 nm and larger are formulated by dispersing anhydrous particles in water. These suspensions are then centrifuged (5000 rpm for 35 min) so as to form a continuous network of particles in contact and to remove most bubbles. This granular paste is then placed in the Petri dish and gelled with the same protocol as above.

Concerning gel synthesis, in the initial state, aggregation of particles is initiated by the addition of NaCl to a concentration of $0.5\,\mathrm{mol\,l^{-1}}$ (for bead diameters smaller than 80 nm) or $MgCl_2$ to a concentration of $0.025\,\mathrm{mol\,l^{-1}}$ (for bead diameters equal to or larger than 80 nm), which ensures

complete gelation after several days. This process simultaneously brings interparticle cohesion by means of liquid phase sintering [26].

Once the samples are gelled, for the smallest beads, 97% of the salt initially incorporated is removed from the system through a special dialysis protocol [25]. The amount of NaCl extracted after each dialysis was evaluated by performing conductivity measurements on dialysates. The remaining concentration of salt within the gels prior drying is about $1\,\mathrm{g\,l^{-1}}$, which ensures, since the solubility of NaCl at 20 °C is $360\,\mathrm{g\,l^{-1}}$, that no crystallization occurs below a saturation of the order of 0.003. For the largest beads no dialysis is carried out and the concentration of salt within the gels prior drying is about $2.4\,\mathrm{g\,l^{-1}}$, which ensures, since the solubility of $MgCl_2$ at 20 °C is $542\,\mathrm{g\,l^{-1}}$, that no crystallization starts before a saturation of 0.004 is reached. Moreover, since the Péclet number [defined as VH/D, where V is the drying velocity (see definition below), H the sample thickness, and D the diffusion coefficient of salt in water] is smaller than 0.1, salt advection can be considered negligible. Finally, since such very low (average) saturations are reached only for the largest beads in the very last stages of drying (see Fig. 1), i.e., when the drying front is close to the sample bottom, we conclude that crystallization will possibly occur in these very last stages, and in a homogenous way throughout the remaining wet region.

After the gelation procedure all our samples were sufficiently rigid to be handled without breaking. The samples with the largest beads were the weakest. At the end of drying, the samples were in a similar state (i.e., rigid). We conclude that the granular material is consolidated; i.e., no relative motion of the particles is expected during the drying process.

Due to the preparation procedure, the samples were *a priori* saturated initially. Visual observation of the fully wet free surface of the sample tends to confirm this statement. The curvature of the initial MRI saturation profiles sometimes observed at the approach of the sample top (see Fig. 1) is not an artifact of the technique. This is essentially due to the initial nonplanar shape of the sample: a meniscus along the peripheral edge and some concavity of the free surface towards the center. On the other hand, the curvature of the profiles at the sample bottom is due to the fact that the Petri dishes were not flat.

The samples were then put to dry inside the MRI magnet. Due to this specific protocol of concentration from a flocculated structure, which might be initially fractal [27], these packings may not be perfectly homogeneous at some scale; e.g., there may remain some larger pores distributed throughout the sample. However, considering the high average volume fraction, the majority of pores must correspond to that expected for a disordered bead packing. Consequently, if such heterogeneities happen to play a role during drying this could only be over a very narrow range of saturations just below 1; in any other situation the drying characteristics rely on the extraction of liquid from the rest of the sample, which can be considered a packing with homogeneous pore size distribution scaling with the particle diameter. Under these conditions the strong interest of these materials is that, *a priori*, since their porous structure remains similar while only one characteristic length scale (i.e., particle size) varies, we can rely on them to allow us to probe the sole effect of pore size on the drying characteristics when it varies from a couple of microns to a few nanometers.

B. Setup

Initially the cylindrical samples are saturated with water; therefore, the solid matrix is completely wet, and only the top surface is open to air. We induce a constant dry air flux (adsorption drying, relative humidity below 0.5%) vertically against the sample free surface at a given flow rate (0.3 m/s), and we follow the drying thanks to NMR measurements (see below). The samples are prepared in Petri dishes of inner diameter 9.6 cm. In some cases the thickness of the material was slightly smaller (by a couple of millimeters) than the height of the dish edge, but this does not significantly affect the drying process or our analysis of the data for the following reasons: the air flux is vertical, which ensures that all the sample surface is reached by this flux; the level difference between the free surface and the top edge of the dish is much smaller than the sample diameter, so the perturbation on the flow is limited to a negligible region at the sample periphery; and for a given sample this

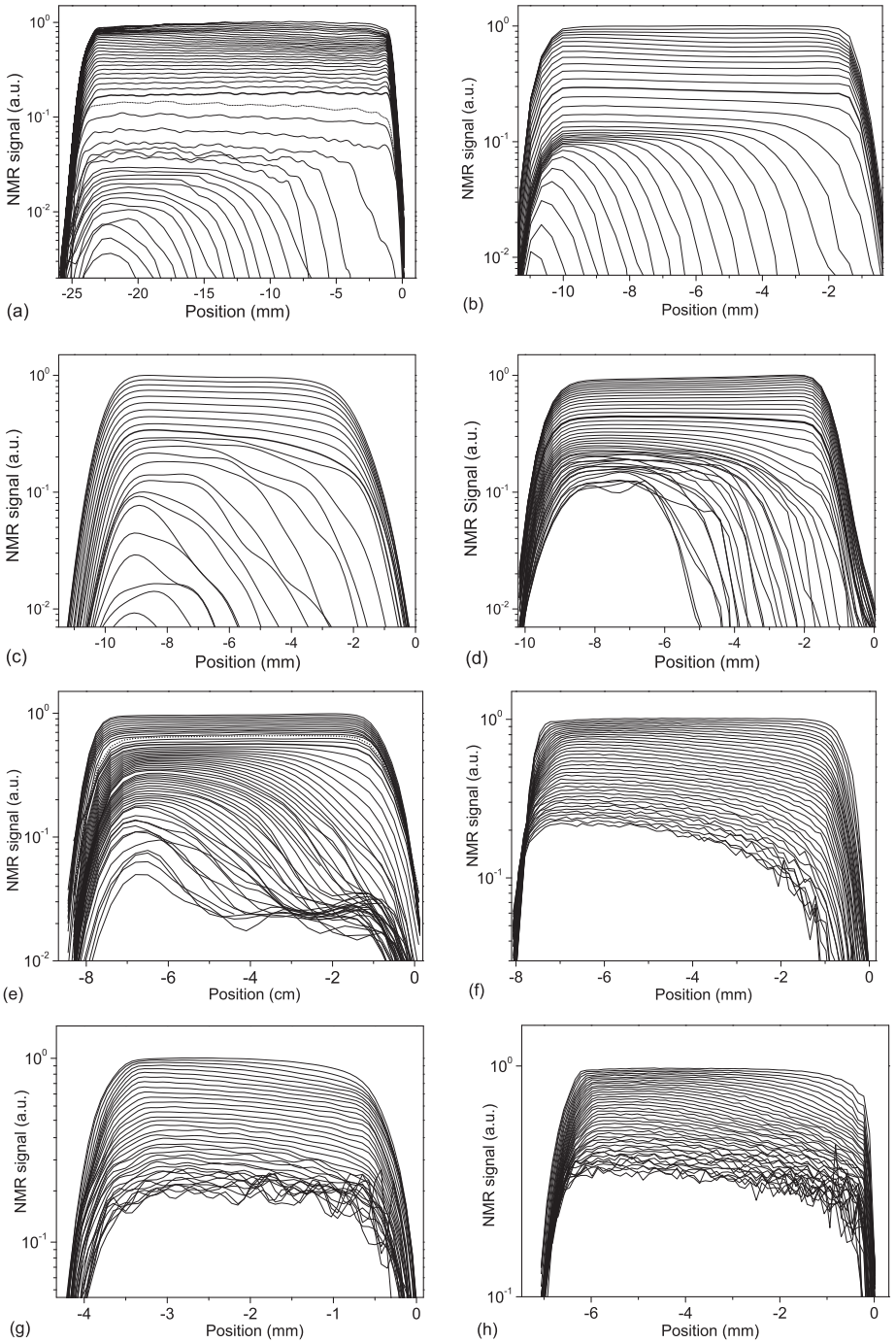

FIG. 1. NMR profiles along sample axis at different times (time interval Δt) (from top to bottom) during drying for bead packings with different particle diameters: (a) 45 000 nm (time interval of 23, then 44 min), (b) 1500 nm (33 min), (c) 1000 nm (36 min), (d) 300 nm (50 min), (e) 80 nm (33 then 44 min), (f) 40 nm (28 min), (g) 12 nm (16 min), and (h) 6 nm (23 min). The first profile with some gradient in saturation is represented by a thicker line. The dotted line corresponds to the first profile after the time interval change. Note that for the sake of clarity data for 300 and 80 nm in the FRP have been smoothened.

potential slight perturbation affects the drying rate in the same way at any time, so our analysis based on a rescaling of the current drying rate by the initial one *a priori* removes the possible impact of this effect.

The sample thickness (H) is in the range 5–10 mm, except for the 45-μm-diam beads (25 mm). Under such conditions the characteristic stress due to gravity ($\rho g H$, with ρ the water density and g the gravity) is smaller than 200 Pa, while the characteristic capillary stress (σ/r, with σ the surface tension and r a typical pore size, say, $r \approx R/3$) is larger than 10 000 Pa. This means that gravity effects are fully negligible in all our tests.

The drying velocity (or drying rate, V) is defined as the equivalent liquid volume crossing the sample free surface cross section per unit time and surface. We thus have $V = -\varepsilon H d\bar{\psi}/dt$, in which $\bar{\psi}$ is the average saturation (ratio of water to pore volume) in the sample and ε the sample porosity ($\varepsilon = 1 - \phi_0$). In order to determine this velocity we rely on NMR measurements (water content profiles in time) that are taken with relatively large time intervals. This explains that we cannot precisely observe the fast decrease in drying rate in the very first times of drying of a porous medium occurring as a result of the evaporation of some liquid layer covering the sample free surface and until the formation of the first liquid meniscus in this region. In the next step, which roughly corresponds to what we could effectively observe from our measurements, the drying rate depends on the interaction between the air flux and the specific shape of the liquid-air interface at the sample free surface, which may depend on the porous medium characteristics. It appears that our imposed air flux induces different initial drying velocities (V_0), decreasing from 0.052 to 0.02 ± 0.004 cm h^{-1} for bead sizes from 45 microns to 6 nm.

Note that previous works showed that the impact of increasing external flux, in terms of the duration of the CRP before reaching the FRP, is qualitatively equivalent to reducing pore size [4]. This means that even if we do not here proceed to systematic tests at different values of external fluxes we can infer that the trends observed when decreasing the pore sizes would be qualitatively similar if the external flux velocity was increased, but the exact variations constitute a field to explore. Moreover, the above statement is *a priori* not valid if the Kelvin effect starts to play a significant role (see below), i.e., for sufficiently small pores and/or saturation.

C. MRI measurements

The distribution of apparent water along the sample vertical axis (z) is measured by placing the sample at the magnetic center of the gradient coil of a 24/80 DBX 0.5-T ^{1}H MRI spectrometer by Bruker (20 cm open diameter in the sample area) and running a one-dimensional double spin-echo measurement (two first echoes of the so-called Carr Purcell Meiboom Gill sequence [25]). An exponential extrapolation was verified and used to compensate for spin-spin relaxation [28]; specifically, the unbiased proton density [$\rho_0(z)$, directly relating to the water content] was extrapolated as $\rho_0(z) = \rho_1(z)^2/\rho_2(z)$, where $\rho_1(z)$ and $\rho_2(z)$ are the signal proton density owing to the first and second echoes, respectively. Although established under the hypothesis of monoexponential relaxation, this type of extrapolation can still be shown to provide a reliable estimate of the amount of water present even in slight multiexponential cases, provided echo times are set short regarding the shortest relaxation time in the sample (in the case of very low sample saturation). Therefore, each measured value of this distribution corresponds to the total amount of water in a thin cross-section layer varying from 75 to 500 μm thickness along the vertical axis of the Petri dish depending on chosen space resolution; we yield the distribution of water in small cross-section layers along the sample axis at different positions and time. Note that the maximum reachable resolution is limited by both sample-induced inhomogeneities of the magnetic field in the MRI magnet and the intrinsic relaxation properties of each sample and therefore may vary from one sample to the other (see [29]).

Eventually, at extremely low proton density the limitation of the dual echo measurement is inevitably reached, which triggers the need to smooth the profiles measured to enhance interpretation of their shape. The smoothing filter we apply corresponds to convolution by means of a Gaussian distribution $g(z) = \exp(-z^2/2\sigma^2)$, with a full width at half maximum σ empirically set to

2.3–4.1 pixels. Since the amplitude of measured profiles may suffer some baseline overestimation at very low signal, this filter is applied to the complex profiles of each echo before its amplitude is treated and prior to extrapolation. Note that when this filter is applied, the resolution of the profile can be considered blurred and the new pixel size increases roughly by a factor of 3.5–6. Data of the order of the noise level were removed.

Note that at the end of their preparation, due to the meniscus effect and the container shape, the sample top and bottom are slightly curved, which induces the appearance of ramps on the profiles, i.e., a progressive decrease of the NMR signal over the millimeter order even if the saturation in the sample is homogeneous (see Fig. 1). The local saturation (ψ) may be obtained by dividing the current local NMR signal by the initial one at the same point (when it exists), but a representation of the NMR signal provides clearer information on the saturation evolution around the top and the bottom of the sample.

III. RESULTS AND DISCUSSION

A. Saturation profiles during drying

The saturation profiles (represented in terms of extrapolated NMR signal, for the reasons explained above) at different times during drying of each sample are shown in Fig. 1. In these figures the first (upper) profile corresponds to a saturated sample and the next ones to a partially saturated sample, with a saturation corresponding to the current ratio of the NMR signal value to the initial value at the same position in the sample. Note that in some cases we adjusted the NMR sequence parameters during the drying, without pausing the experiment, to optimize the resolution and reduce the noise level; this could be performed a couple of times during the same experiment and explains some variations in the aspect (spacing, smoothness) of the series of profiles with time. The reproducibility of these data has been verified by repeating several of these tests up to three times. Some slight differences could be observed in the exact evolution of the shape of the profiles, especially at low saturation, but within the frame of our analysis this is negligible. Our representation of these profiles in logarithmic scale is allowed thanks to the good signal to noise ratio of our data, which thus provides information concerning the distribution of liquid water in the samples down to a saturation of 0.1% for the beads larger than 1 micron. Obviously, the smallest saturation observed increases as the beads become smaller, since the thickness of the liquid films reaches the molecular size at larger saturation (we analyze this point further below).

For bead sizes down to 80 nm we observe a first period during which, while decreasing, the saturation remains almost perfectly homogeneous: in a logarithmic scale the profiles remain strictly parallel [see Figs. 1(a)–1(e). This means that although water is withdrawn in the form of vapor from the top surface of the sample a balance of capillary effects is maintained throughout the sample whatever the value of the average saturation in this regime. Thus, as air enters the sample, there is a liquid "counterflow" directed towards the sample free surface which makes it possible to keep a uniform (Laplace) pressure throughout the sample, an effect already identified in the literature [4,30,31]. However, as a result of the increasing withdrawal of liquid in the top layers of the sample, this liquid motion occurs in the form of successive bursts of capillary reequilibration throughout the complex disordered medium [16,32,33]. A recent pore network modeling, which proved to be able to well predict the CRP characteristics and the occurrence of the second stage, provides a further view of the physical effects at a local scale [34]. Note that it was also proved from simple mass conservation arguments that, if the saturation decreases homogeneously in time, the liquid velocity increases linearly from the bottom to the top of the sample [34].

Within some uncertainty on the exact moment of its onset (i.e., first homogeneous partially saturated state), and even if, sometimes, significant fluctuations are observed during that period, this regime is essentially associated with a constant drying rate. This so because (i) At a very short distance from the first liquid-air interface the vapor density is at its maximum and likewise in depth, as the air pockets are surrounded by liquid-air interfaces; consequently, evaporation mainly

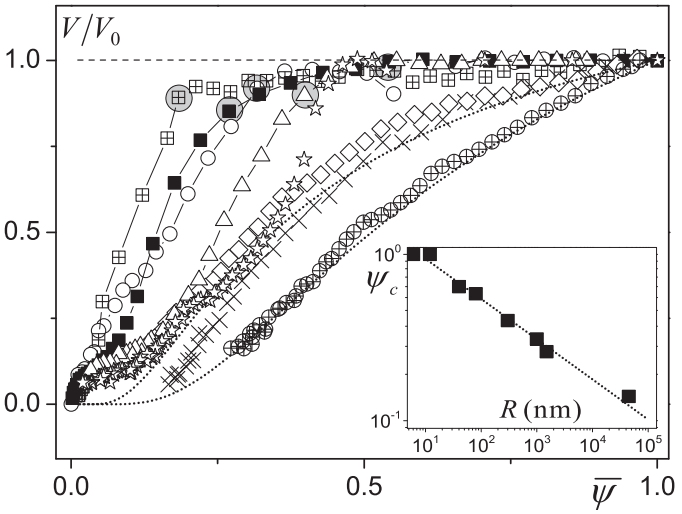

FIG. 2. Drying velocity (rescaled by the initial one) as a function of the saturation for bead packings with different bead diameters: 45 000 nm (cross squares), 1500 nm (solid squares), 1000 nm (circles), 300 nm (triangles), 80 nm (stars), 40 nm (diamonds), 20 nm (crosses), 6 nm (cross circles). The position of the first MRI profile (see Fig. 1) with saturation gradient is shown with a grey disk. The dotted lines correspond to the model based on the Kelvin effect (see text). The inset shows the critical saturation, associated with the formation of a gradient in the saturation profile, as a function of the particle radius. The dotted line in the inset corresponds to $\psi_c = 1.8R^{-1/4}$, with R in nanometers.

occurs from the first liquid-air interface (around the sample free surface) where a significant vapor density gradient is expected [35]. (ii) The liquid transport towards the free surface maintains a set of liquid-air interfaces (liquid patches) in that region, which in turn can maintain a (constant) maximum vapor density around almost the same position below the air flux so that the boundary conditions for evaporation remain constant [36,37].

Below some critical saturation (ψ_c), a saturation gradient appears below the sample free surface (see Fig. 1); i.e., the corresponding saturation profile is no longer parallel to the previous one. Around the same time the drying rate starts to decrease (see the grey disks in Fig. 2). This occurs sooner (i.e., for larger ψ_c) for smaller bead radius.

For the largest beads ($\geqslant$40 nm), we can then observe the development of a region, just below the free surface, where the saturation profiles drop to very small values [not larger than the noise; see Figs. 1(a)–1(d)]. This may be considered an apparent dry region, i.e., one from which no more liquid can be extracted, and we measure the thickness of this region (h) from the NMR saturation profiles. Note, however, that this apparent dry region in fact corresponds to a region where no NMR signal larger than the noise could be detected. The corresponding critical liquid content, i.e., that below which no relevant signal can be measured, depends on the sample relaxation characteristics along with our NMR parameters chosen; however, measurement of the dry mass of the samples (after 24 h spent in the oven postdrying) confirmed a negligible residual amount of water. The strong drop in saturation observed in logarithmic scale around some positions in our profiles (see Fig. 1) anyway suggests that if there remains some liquid in the apparent dry region its thickness is very small, of the order of the molecular size. It happened that for the 80-nm beads the NMR parameters allowed us to also get relevant measurements in this region [see Fig. 1(e)]: there we see an apparent uniform level from the front of the dry region to the free surface of the sample. In order to estimate the typical thickness (e) of the liquid films let us assume that the liquid present in the porous medium is equally distributed at the surface of the beads. In that case, we have $4\pi eR^2/(4\pi R^3/3) = (1-\phi_0)\psi/\phi_0$, so

that $e \approx 0.24 R\psi$. We find a plateau at a saturation around 3%, which corresponds to an average liquid film thickness of 0.29 nm, of the order of the water molecule diameter (0.34 nm).

This suggests that there remains a molecular thick layer adsorbed on the solid surface, even in a region usually assumed to be dry, in the ultimate stages of sample drying under convection, possibly resulting from an adsorption equilibrium with the residual water contained in the "dry air" flow. This is confirmed by the data for smaller bead sizes [see Figs. 1(f)–1(h)]. Here the profiles appear to become very noisy and almost stagnant, below a saturation around the critical value for which, according to the above formula, the liquid film thickness is of the order of the molecule size. As the next profiles were greatly affected by the measurement noise, we skipped their representation. This rapid development of the noise in fact suggests that the number of mobile liquid water molecules tends to zero, except for a thin layer of poorly mobile adsorbed water molecules on the solid surface.

For the 40-nm-diam beads a dry front starts to develop from the very beginning of drying [see Fig. 1(f)], apparently in the continuity of the observations for larger beads. However, the drying front eventually does not spread very deep and its position seems to reach an asymptotic value while the rest of the sample desaturates almost homogeneously. For smaller beads no more dry front appears; the sample immediately desaturates almost homogeneously [see Figs. 1(g) and 1(h)]. Thus it appears that the drying characteristics of nanoporous materials exhibit specific trends. This is not so surprising as we are here dealing with materials with a pore size of the order of a few molecules. For example, for the 12-nm beads, the typical pore size is 2 nm, which is six times the molecule size. In that case, the concept of thermodynamic phase is not relevant, so one cannot expect that some liquid could simply drain towards the sample free surface as a result of standard capillary effects [38]. It is remarkable that for nanopores there is apparently an effect playing a similar role, thus allowing homogeneous desaturation of the sample during drying.

B. Drying rate

Let us attempt to quantify the evolution of the drying rate according to these observations. Just before the transition between CRP and FRP the relative humidity n is equal to 1 at the sample free surface and drying may be described as vapor diffusion, from the air-liquid interface, through a boundary layer (of air) of thickness δ, and up to a region where $n = 0$. Under such conditions, from the Fick's second law, we obtain $V_0 = (\rho_0/\rho) D_0/\delta$, with $D_0 = 2.7 \times 10^{-5}\,\mathrm{m^2\,s^{-1}}$ the water vapor diffusion coefficient in air, and $\rho_0 = 23.4\,\mathrm{g\,m^{-3}}$ the maximum vapor density in air (at 25 °C). Later on, when a dry region has developed inside the sample from its free surface, we can still assume for the sake of simplicity that the liquid evaporates exactly from the limit of the wet region (where $n = 1$) and the vapor diffuses to the free surface over a distance h, i.e., the thickness of the dry region, before reaching the external boundary layer. Now the relative humidity at the sample free surface is n_1 and the drying velocity is $V = n_1 \rho_0 D_0/\rho\delta = n_1 V_0$. In addition, the vapor density gradient along the dry region induces a vapor flux which can be expressed in steady state as $V = \rho_0 D_v (1 - n_1)/\rho h$, where D_v is the vapor diffusion coefficient through the (dry) porous medium. We can write D_v as $\varepsilon D_0/\tau$, where τ the tortuosity of the medium [30]. Note that in this description D_v appears independent of the bead size, which translates into the assumption of the kinetics of vapor diffusion not being affected by pore size.

From the two above expressions for the vapor flux we deduce $n_1 = 1/(1 + D_0 h/D_v \delta)$, and the drying rate can be written as $V = \rho_0 D_v/\rho(h + \delta^*)$ with $\delta^* = D_v \delta/D_0$. This may be rewritten as

$$[(V_0/V) - 1] = (\rho/\rho_0 D_v) h V_0. \tag{1}$$

Let us compare this theoretical prediction with our data. In this frame the most difficult point is the determination of h. Since in logarithmic scale the saturation profiles exhibit a vertical asymptote at some distance from the sample top, it is natural to consider this distance as the thickness of the dry front. However, in such profiles, we ignore if the saturation gradient, which progressively extends over a longer distance as the dry front progresses, is due to a homogeneous variation of the saturation in the sample or to some heterogeneity of the advancing front structure. Finally, we ignore if the

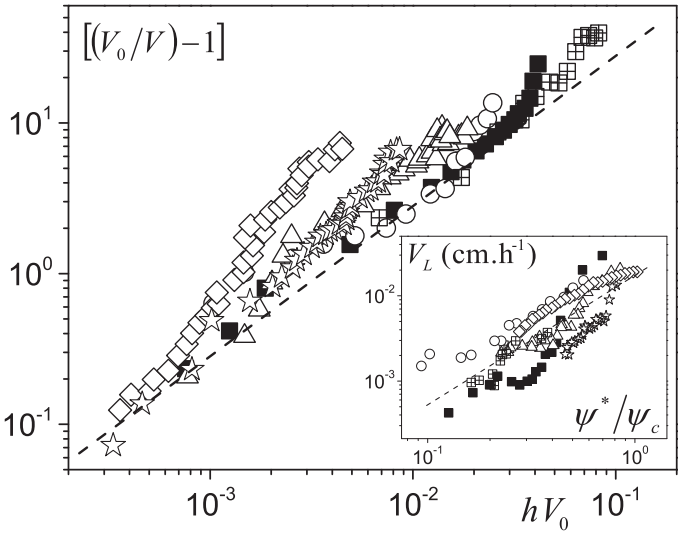

FIG. 3. Evolution of a function of the rescaled velocity (which may also be seen as the deviation from the drying rate in the CRP) as a function of the thickness of the dry front times the initial velocity for the different bead sizes (same symbols as in Fig. 2). Dotted line has a slope of 1. The inset shows the mean liquid velocity in the wet region as a function of the mean saturation in this region.

position at which we should consider that $n = 1$ is situated at the vertical asymptote or at some distance behind, within the saturation gradient. For the calculations here, we keep the first option.

For $R \geqslant 40$ nm we observe a first stage during which the data plotted in terms of $[(V_0/V) - 1]$ vs hV_0 effectively follow a master curve of slope 1, in a larger range of dry region thickness when the bead radius increases (see Fig. 3); this period lasts for up to two decades of dry front thickness for the largest beads, in agreement with the prediction of Eq. (1). Therefore, our measurement of the height of the dry region from the position of the NMR profile appears consistent, as well as the assumption of a unique diffusion coefficient through these similar porous media down to slightly more than diameters of 300 nm. In this regime, the value for D_v extracted from the straight line fitted to this master curve corresponds to a tortuosity $\tau = 2.5 \pm 0.2$, which is significantly larger than the ratio of the length of the effective path of a molecule to skirt the grain to its diameter, i.e., $\pi/2 \approx 1.6$. This suggests that the effective position for which $n = 1$ is in fact situated at some slight distance behind, in the region of saturation gradient, by a more or less constant factor (say, between 1.2 and 1.5) which would shift the data of Fig. 3 to the right, leading to a larger diffusion coefficient and a smaller tortuosity.

Despite this difficulty, the variations are as expected from the theory, so these results confirm the consistency of a description of drying in porous media in a wide range of pore sizes in two stages: a CRP followed by a FRP during which a dry front recedes and the drying rate results from vapor diffusion from the dry front. Additionally, this analysis shows that even if there may remain some adsorbed liquid layer on the beads in this dry region, not detected by our NMR measurements, it does not play a significant role in drying process.

From 300 nm and smaller diameters we observe a progressively larger deviation of the data from the master curve, constituting a second stage in the evolution of the development of the apparent dry region. Since the physical scheme of regime 1 appeared valid at larger diameters it is natural to consider that some specific effect due to the small pore size could play a more and more important role as the diameter decreases. In this context, one may think of an impact of the Knudsen effect for bead diameter less than 1 μm since in this case the pore size is not much larger than the mean free path of the water molecules (i.e., $l \approx 80$ nm under a pressure of 1 atm), which is known to affect the

coefficient of diffusion. As a first approximation, we can describe this effect over the whole range of pore sizes by considering that the diffusion coefficient is in fact $D = \xi D_v$, with $\xi = (1 + l/L)^{-1}$ [39]. This shows that this effect should tend to shift the data as a whole above the theoretical curve (i.e., towards lower values of hV_0) in Fig. 3, by a factor depending on the bead size but independent of other characteristics (dry region thickness, saturation, etc). We ignore the exact value of L for a porous medium (for a straight channel this is the channel diameter) but if it was of the order of the typical pore size the coefficient ξ would be significantly smaller than 1 for $R \leqslant 300$ nm. This is not what we observe: the data first follow a curve of slope 1, approximately independent of R, for small h values, then they start to depart from this curve by a coefficient increasing with h (see Fig. 3). Finally, there is a clear departure from a straight line of slope 1 for small R, as clearly appears for $R = 40$ and $R = 80$ nm. Thus, it seems like the Knudsen effect alone fails to describe our observations, and the major effect of significant decrease of the drying rate for the observed dry region thickness, becoming more important as the saturation decreases, has to be explained by other means.

Actually another effect may be at the origin of the deviation from our simple theory above. Let us first recall that this deviation occurs earlier, and thus at larger saturation, for decreasing particle diameter. Moreover, for smaller beads, namely, 6 and 12 nm diameter, no dry front at all can be observed, whereas the drying rate decreases to zero (see Fig. 2). This may be considered as being in the continuity of the effect observed at larger size: for very small bead size the slope in Fig. 3 would simply be vertical (i.e., constant h for increasing V). The original characteristics of drying for such small pores, i.e., an almost homogeneous desaturation with a significantly decreasing drying rate, suggests that our assumption concerning the vapor density value along the first wet interface is not valid here.

The origin of this feature is likely the Kelvin effect [39], which predicts that, if water vapor behaves as a perfect gas, in a medium in contact with a curved liquid-air interface the saturation vapor pressure is smaller than otherwise. The phenomenon finds its origin in the equality of the thermodynamic potential of the liquid, proportional to the pressure here equal to σ/r, where σ is the surface tension and r is the radius of curvature of the interface, with that of the gas, proportional to $\ln n_r$, where n_r is the relative humidity along a liquid-air interface. Under our experimental conditions this leads to $n_r = \exp -\frac{\sigma\Omega}{RT}(\frac{1}{r}) \approx \exp -0.54/r$, with Ω the water molar volume, R the gas constant, T the temperature in kelvins, and r expressed in nanometers. Note that the application of this calculation to a porous medium with complex and heterogeneous local liquid-gas interface shape is an approximation. From this estimation, we deduce that this effect becomes significant ($1 - n_r > 10\%$) for $r < 5$ nm. If we now simply assume again that evaporation mainly occurs around the most external liquid-air interface for nanoporous media which apparently remain wet up to the free surface (see Fig. 1), we get a drying rate equal to $V_r = n_r \rho_0 D_0/\rho\delta$, which may be significantly lower than otherwise.

To compare this hypothesis to our results in a more accurate manner, we have to determine r as a function of the current (mean) saturation. We simply assume that, in the range of saturations [0.3–1] r varies like the thickness of the liquid films inside the sample, i.e., it is essentially proportional to R and ψ. Since we also know that it tends to infinity when $\psi \to 1$ and is of the order of the pore size (proportional to R) when $\psi \approx 0.5$, an expression which well reproduces all these trends is $r = \zeta R\psi/(1 - \psi)$. The factor ζ allows one to express the exact pore size value to be taken into account around the most external liquid-air interfaces, i.e., resulting from the saturation gradient at the approach of the free surface of the sample. Using this expression for r in the above drying rate equation we can compute the evolution of the relative drying rate (V_r/V_0) as the saturation decreases. Remarkably, with this model, we are able to reproduce very well the data for 6 and 12 nm with a single factor $\zeta = 1/4$ (see Fig. 2), which corresponds to a value for r close to a typical pore radius at $\psi \approx 0.5$, which seems in reasonable agreement with what we can expect when removing half the liquid volume from a bead packing. Note that this description assumes that for these nanoparticles most evaporation essentially occurs close to the top surface of the sample, which is certainly the case considering the almost homogeneous saturation profiles which imply that (even with the Kelvin

effect) the vapor density gradient inside the medium will be very small. Finally our description assumes that capillary effects again play a major role. However, as we already remarked, when the liquid thickness is only a few times the molecule size, it remains unclear how with such effects one can still obtain a phenomenon of equilibration of the thickness of the liquid layer throughout the sample at any time during drying. Under such conditions our description through the Kelvin effect associated with reequilibrium may only be seen as a convenient simple approach in agreement with data.

Indeed, the Kelvin effect should *a priori* also take place during the drying of samples with larger pore sizes, since, as the saturation decreases, the liquid film thickness—and correspondingly the curvature radius of the menisci—decreases. According to the above estimations a significant impact of this effect should be observed for a saturation such that this radius of curvature is of the order of or below about 5 nm. Typically, with 40-nm bead diameter, the pore size is of the order of 6 nm (from geometrical estimations), so the radius of curvature of the menisci is of the same order at the beginning of drying. Thus, a significant decrease of drying rate as the saturation decreases is expected soon after the beginning of drying. For 80-nm beads a significant deviation can be expected below a saturation of the order of 40%, and for 300 nm, below about 10%. These estimations seem consistent with the starting points of deviation from the basic theory, observed in Fig. 2.

C. Analysis of flow in the wet region

Since we now have a clear view of the origin of the drying rate evolution as a function of the liquid distribution in time inside the sample it is interesting to see if we can predict this distribution and its evolution in time. Let us consider the receding front regime. Our data, providing rather precise information at low saturation, show that in contrast with some previous assumptions [4,17–19] this regime does not simply correspond to a growth of the apparent dry region. Indeed even when this region occupies a significant fraction of the sample the saturation in the wet region goes on decreasing almost homogeneously, more or less as in the CRP regime (but now with a significant saturation gradient at the approach of the dry region), and this is so down to extremely low saturation, approaching the minimal observable value [see Figs. 1(a)–1(f)]. For example, in Fig. 1(b) one may see that, for a saturation in the range 0.1–0.2, the dry front recedes significantly while the saturation decreases homogeneously over some significant sample thickness. In this context a critical question concerns the way the fluid is transported inside this wet region. Indeed we can consider two very different situations: a transport as liquid films through a connected network or a transport as vapor through the pores.

A transport as vapor is possible only if a significant gradient of saturation exists. As a matter of fact, such a gradient induces a gradient of liquid meniscus curvature, leading to a gradient of vapor density at equilibrium with the liquid (Kelvin effect). We write the spatial variation of saturation, $\Delta\psi$, and the corresponding variation of vapor density, Δn. Only then, a Fickian diffusion through the voids of the wet region (of thickness d) may occur. Let us estimate the drying rate associated with this process. It is equal to $V_g = \Delta n \rho_0 D_v'/\rho d$, in which $D_v' \approx (1-\psi)D_v$. This transport is significant if the value of V_g is of the order of the drying rate of the sample, which was shown (see above) to be well estimated by considering vapor diffusion from the upper layers of the wet region, expressed as $V = n_r \rho_0 D_v/\rho(h+\delta^*)$. Thus, we have $V_g/V = (\Delta n/n_r)(1-\psi)(h+\delta^*)/d$, which may also be written $V_g/V \approx (d \ln n)(1-\psi)(h+\delta^*)/d$. Note that from the measured drying rate we know that δ^* is of the order of 1 mm. Assuming equilibrium and using again our above approximate expression for r we have $1/r \approx 4(1-\psi)/R\psi$, so that we get $V_g/V \approx 2(1-\psi)\Delta\psi(h+\delta^*)/R\psi^2 d$, in which R is expressed in nanometers. We can estimate this ratio from our data for the different bead sizes, by using values for the saturation, the thickness of the wet and dry regions, as they can be measured from Fig. 1. For bead diameters between 300 and 45 000 nm, the maximum value for the ratio $(h+\delta^*)/d$ is of the order of 5, and the maximum value for the saturation variation $\Delta\psi$ is of the order of 20% of ψ, so that in the domain where one can still observe an apparent plateau (in fact a region of slow spatial variations) of ψ in the wet region (typically for $\psi > 0.1$ except for the largest beads), we have. For the 80-nm beads, or for larger beads in the region of significant saturation

gradient (either at the top of the wet region or in the very last stages of drying observed in our tests), we may find larger values for this ratio, typically of the order of 1, and the vapor transport through the wet region might be significant. Finally for smaller bead radii, in our range of observation, $\Delta\psi$ is of the order of 0.1, ψ of the order of 0.5, and $h + \delta^*/d$ of the order of $1/5$, so that V_g/V is much smaller than 1 and vapor transport in the wet region is negligible.

We conclude that except for a narrow range of radii or in the ultimate stages of drying when water remains in the bottom layers of the sample, evaporation from inside the wet region and then transport towards the upper layers is negligible; however, by no means is the vapor transport significant in the homogeneously saturated regions. This implies that, to explain the desaturation of the wet region below the dry front, there must exist a continuous liquid network, made of liquid films possibly with liquid bridges at contact points, through which a significant transport process occurs. Under these conditions, here again, the homogeneous saturation decrease is associated with some capillary reequilibration processes. However, in contrast with the regime of initial homogeneous saturation decrease throughout the sample and associated with a constant drying rate, here the liquid transport velocity induced by the capillary effect is no longer sufficient to provide a liquid amount as large as that removed by evaporation. This explains that we now have at the same time an inward displacement of the dry front and a homogeneous desaturation in the wet region. Thus, the dry front progression results from some balance between evaporation and liquid flow in the wet region. In the following we focus on this liquid transport.

Thanks to our data providing a view of the liquid distribution in time we can get some information on the flow characteristics inside the wet region. More precisely we can compute the characteristic velocity of the liquid phase in this region. We focus on the liquid velocity through the upper section of the wet region. Since in the homogeneous saturation regions below the dry front the same approach based on mass conservation used for the CRP (see above) would show that the liquid velocity varies linearly with the distance, the velocity in each position is simply proportional to the velocity through the upper surface of the wet regions. In that aim we describe the liquid content in this region with the help of an average saturation ψ^* which, from the liquid mass conservation, is such that $H\bar{\psi} = (H - h)\psi^*$. Deriving this equation we deduce the expression for the mean velocity of the liquid phase per unit surface, $V_L = -\varepsilon(H - h)(d\psi^*/dt) = V - \varepsilon\psi^*(dh/dt)$, which is represented in the inset of Fig. 2. Considering the gradient of saturation extending over a significant sample thickness in the FRP regime it is tempting to assume that the liquid flow can simply be described by Darcy's law for a partially saturated flow through a porous medium under the effect of a pressure gradient. This gives a velocity $V_L = -(k/\mu)\nabla p$, where ∇p is the pressure gradient, μ the liquid viscosity, and k the permeability of the liquid network (unsaturated porous medium). The typical pressure is the Laplace pressure $p = \sigma/r(\psi^*)$, where $r(\psi^*)$ is the mean radius of curvature of the liquid-air interface in the region of saturation ψ^*. $r(\psi^*)$ scales with the bead radius and it may be shown from basic geometrical considerations that at low saturation the radius of curvature of the interface around the points of contact between the grains is proportional to $\sqrt{\psi^*}$. The typical length scale for the extent of pressure variation is the sample thickness H. On the other hand, we know that the permeability k scales with the square of the mean liquid channel thickness (e) via a constant factor of the structure, for example equal to $1/8$ for straight parallel ducts. e is equal to the ratio of the liquid volume per bead, i.e., $4(\varepsilon/1 - \varepsilon)\pi R^3\psi^*/3$, and to the corresponding solid area, i.e., $4\pi R^2$, which gives $e = uR\psi^*$ with $u = \varepsilon/1 - \varepsilon$ (ε being the porosity), so that we write $k = \beta R^2\psi^{*2}$, where β is a characteristic of the porous structure. We finally get

$$V_L \propto (\sigma/\mu H)\psi^{*1.5}R. \tag{2}$$

Our data show an approximate scaling of the type $V_L \propto (\psi^*/\psi_c)^{1.5}$ in agreement with this expression (see inset of Fig. 3) concerning the variation with ψ^*. However, here the dependence on R is only expressed through the variation with ψ_c. Indeed, in the representation of the inset of Fig. 3 the data for $V_L(\psi^*/\psi_c)$ are situated in a narrow area without any apparent monotonous variation of their level with R. Since $\psi_c \propto R^{-1/4}$ (see inset of Fig. 2) we thus deduce essentially

$V_L(R) \propto {\psi_c}^{-1.5} \propto R^{0.37}$. This means that the expected scaling as R of Eq. (2) does not apply at all over our four-decade range of pore sizes. This suggests that the "classical hydrodynamic description" assumed above is not appropriate in this context.

Actually, this result might be due to the specific process of capillary reequilibration in the CRP, assumed to be similar in the FRP in the wet regions where the saturation remains homogeneous. As already mentioned this process relies on successive steps of redistribution of saturation throughout the medium, allowing the Laplace pressure to be uniform at any time between two such events. So it does not seem clear that this process is equivalent to a flow on average governed by a simple gradient of Laplace pressure along the main flow direction through an (almost) constant liquid network. Instead, there might be strong variations of the local Laplace pressure between two successive reequilibration events throughout the medium. These variations of the driving force could finally induce some different average hydrodynamic behavior of the system.

IV. CONCLUSION

NMR provides a robust approach to the study of confined liquid flow down to the molecular scale by averaging over a macroscopic sample. Investigating drying on a variety of model porous media through dynamic MRI measurements provided us with saturation profiles in time down to molecular liquid film and close to complete evaporation for a wide range of pore sizes. Consistent with what was so far essentially shown for packings of relatively large beads, a CRP associated with homogeneous desaturation is shown to exist down to bead sizes of a few hundred nanometers. A falling rate period then occurs as an apparent dry region develops. During that stage, we verified the variations in the drying rate being governed by the diffusion of vapor through the apparent dry zone. For small pore sizes one could expect the impact of the Knudsen effect, inducing a decrease of the diffusion coefficient when the pore size decreases, due to the increasing collision rate of gas molecules to the matrix walls. However, such an effect was not clearly observed in our tests. Finally, the drying rate proved essentially to be increasingly reduced because of the effect of interface curvature, i.e., the Kelvin effect. In particular, we demonstrated that the former effect fully governs the kinetics of drying in nanoporous media for which, surprisingly, a homogeneous desaturation is observed whereas standard capillary effects can hardly play a major role in this situation.

This study especially reveals that the saturation decreases approximately homogeneously throughout the wet regions of the material even if a dry front develops. This proves the existence of a continuous liquid network capable of draining towards the interface of higher evaporation all along drying and whatever the pore size. This phenomenon results from capillary reequilibration effects as in the CRP. In this framework, we proved that the scaling with the pore size expected when assuming that the liquid is transported upwards through its own network driven by a standard value of the Laplace pressure does not correspond to our data.

Our results show that the flow of liquid in drying porous media exhibits original trends, and complex effects start to play a role for very small pores, which need to be further studied. This might in particular provide complementary information to the usual studies concerning the properties of thin liquid films (at a scale of the order of the nanometer). We also showed that capillary reequilibration effects play a major role at any time during drying, even at extremely low saturation, i.e., with thin liquid films. This phenomenon is poorly known and should be further studied to reach a full description of the processes occurring during drying: in particular, the transition from the CRP to the FRP and during the FRP.

[1] J. Van Brakel, Mass transfer in convective drying, Adv. Drying **1**, 217 (1980).

[2] J. B. Laurindo and M. Prat, Numerical and experimental network study of evaporation in capillary porous media, Chem. Eng. Sci. **53**, 2257 (1998).

[3] I. N. Tsimpanogiannis, Y. C. Yortsos, S. Poulou, N. Kanellopoulos, and A. K. Stubos, Scaling theory of drying in porous media, Phys. Rev. E **59**, 4353 (1999).
[4] P. Coussot, Scaling approach of the convective drying of a porous medium, Eur. Phys. J. B **15**, 557 (2000).
[5] F. Chauvet, P. Duru, S. Geoffroy, and M. Prat, Three Periods of Drying of a Single Square Capillary Tube, Phys. Rev. Lett. **103**, 124502 (2009).
[6] D. Or, P. Lehmann, E. Shahraeeni, and N. Shokri, Advances in soil evaporation physics—A review, Vadose Zone J. 12 (2013).
[7] N. Prime, Z. Housni, L. Fraikin, A. Leonard, R. Charlier, and S. Levasseur, On water transfer and hydraulic connection layer during the convective drying of rigid porous material, Transp. Porous Media **106**, 47 (2015).
[8] P. Coussot, C. Gauthier, D. Nadji, J. C. Borgotti, P. Vié, and F. Bertrand, Capillary motion during drying of a granular paste, C.R. Acad. Sci., Paris **327**, 1101 (1999).
[9] L. Pel, H. Brocken, and K. Kopinga, Determination of moisture diffusivity in porous media using moisture concentration profiles, Int. J. Heat Mass Transfer **39**, 1273 (1996).
[10] P. Faure and P. Coussot, Drying of a model soil, Phys. Rev. E **82**, 036303 (2010).
[11] G. H. A. van der Heijden, L. Pel, H. P. Huinink, and K. Kopinga, Moisture transport and dehydration in heated gypsum, an NMR study, Chem. Eng. Sci. **66**, 4241 (2011).
[12] A. Yiotis, D. Salin, E. Tajer, and Y. Yortsos, Drying in porous media with gravity-stabilized fronts: Experimental results, Phys. Rev. E **86**, 026310 (2012).
[13] P. Lehmann, S. Assouline, and D. Or, Characteristic lengths affecting evaporative drying of porous media, Phys. Rev. E **77**, 056309 (2008).
[14] N. Shokri, P. Lehmann, P. Vontobel, and D. Or, Drying front and water content dynamics during evaporation from sand delineated by neutron radiography, Water Resour. Res. **44**, 06418 (2008).
[15] N. Shokri and D. Or, What determines drying rates at the onset of diffusion controlled stage-2 evaporation from porous media? Water Resour. Res. **47**, W09513 (2011).
[16] N. Grapsas and N. Shokri, Acoustic characteristics of fluid interface displacement in drying porous media, Int. J. Multiphase Flow **62**, 30 (2014).
[17] N. Ceaglske and O. A. Hougen, Drying granular solids, Trans. Am. Inst. Chem. Eng. **33**, 283 (1937).
[18] S. Whitaker and W. T. H. Chou, Drying granular porous media-theory and experiment, Drying Technol. **1**, 3 (1983).
[19] P. Chen and D. C. T. Pei, A mathematical model of drying processes, Int. J. Heat Mass Transfer **32**, 297 (1989).
[20] N. Shahidzadeh-Bonn, A. Azouni, and P. Coussot, Effect of wetting properties on the kinetics of drying of porous media, J. Phys.: Condens. Matter **19**, 112101 (2007).
[21] M. D. Seck, E. Keita, P. Faure, P. Cavalié, M. Van Landeghem, S. Rodts, and P. Coussot, Subflorescence and plaster drying dynamics, Chem. Eng. Sci. **148**, 203 (2016).
[22] E. Keita, P. Faure, S. Rodts, and P. Coussot, MRI evidence for a receding-front effect in drying porous media, Phys. Rev. E **87**, 062303 (2013).
[23] E. Keita, T. E. Kodger, P. Faure, S. Rodts, D. A. Weitz, and P. Coussot, Water retention against drying with soft-particle suspensions in porous media, Phys. Rev. E **94**, 033104 (2016).
[24] J. Thiery, E. Keita, S. Rodts, D. Courtier Murias, T. Kodger, A. Pegoraro, and P. Coussot, Drying kinetics of deformable and cracking nano-porous gels, Eur. Phys. J. E **39**, 117 (2016).
[25] J. Thiery, S. Rodts, E. Keita, X. Chateau, P. Faure, D. Courtier-Murias, T. E. Kodger, and P. Coussot, Water transfer and crack regimes in nanocolloidal gels, Phys. Rev. E **91**, 042407 (2015).
[26] G. C. Kuczynski, Study of the sintering of glass, J. Appl. Phys. **20**, 1160 (1949).
[27] D. A. Weitz and M. Oliveria, Fractal Structures Formed by Kinetic Aggregation of Aqueous Gold Colloids, Phys. Rev. Lett. **52**, 1433 (1984).
[28] *Signal Treatment and Signal Analysis in NMR*, edited by D. N. Rutledge (Elsevier Science, New York, 1996), Vol. 18.
[29] P. T. Callaghan, *Principles of Nuclear Magnetic Resonance Microscopy* (Clarendon, Oxford, UK, 1993).
[30] T. M. Shaw, Drying as an Immiscible Displacement Process with Fluid Counterflow, Phys. Rev. Lett. **59**, 1671 (1987).

[31] A. G. Yiotis, A. G. Boudouvis, A. K. Stubos, I. N. Tsimpanogiannis, and Y. C. Yortsos, Effect of liquid films on the drying of porous media, AIChE J. **50**, 2721 (2004).
[32] L. Xu, S. Davies, A. B. Schofield, and D. A. Weitz, Dynamics of Drying in 3D Porous Media, Phys. Rev. Lett. **101**, 094502 (2008).
[33] J. Thiery, Water transfers in sub-micron porous media during drying and imbibition, Ph.D. thesis, Université Paris-Est, 2016.
[34] A. A. Moghaddam, A. Kharaghani, E. Tsotas, and M. Prat, Kinematics in a slowly drying porous medium: Reconciliation of pore network simulations and continuum modeling, Phys. Fluids **29**, 022102 (2017).
[35] E. Keita, S. A. Koehler, P. Faure, D. A. Weitz, and P. Coussot, Drying kinetics driven by the shape of the air/water interface in a capillary channel, Eur. Phys. J. E **39**, 23 (2016).
[36] M. Suzuki and S. Maeda, On the mechanism of drying of granular beds, J. Chem. Eng. Jpn. **1**, 26 (1968).
[37] P. Lehmann and D. Or, Effect of wetness patchiness on evaporation dynamics from drying porous surfaces, Water Resour. Res. **49**, 8250 (2013).
[38] B. Coasne, A. Galarneau, R. J. M. Pellenq, and F. Di Renzo, Adsorption, intrusion and freezing in porous silica: The view from the nanoscale, Chem. Soc. Rev. **42**, 4141 (2013).
[39] J. F. Daian, *Equilibrium and Transfers in Porous Media* (Wiley, New York, 2014).